Inorganic Chemistry

pubs.acs.org/IC Article

Bi^{3+}-Doped $BaYF_5$:Yb,Er Upconversion Nanoparticles with Enhanced Luminescence and Application Case for X-ray Computed Tomography Imaging

Ran Luo, Lei Chen, Qinyu Li, Jie Zhou, Linqiang Mei, Zhanglei Ning, Yan Zhao,* Mengjiao Liu, Xin Lai, Jian Bi, Wenyan Yin,* and Daojiang Gao*

Cite This: https://dx.doi.org/10.1021/acs.inorgchem.0c01818 Read Online

ABSTRACT: In this work, $BaYF_5$:20%Yb^{3+}/2%Er^{3+}/x%Bi^{3+} (abbreviated as $BaYF_5$:Yb,Er,Bi_x, where x = 0−3.0) upconversion nanoparticles (UCNPs) with various doping concentrations of Bi^{3+} were synthesized through a simple hydrothermal method. The influence of the doping amount of Bi^{3+} on the microstructures and upconversion luminescence (UCL) properties of the $BaYF_5$:Yb,Er,Bi_x UCNPs was studied in detail. The doping concentration of Bi^{3+} has little influence on the microstructures of the UCNPs but significantly impacts their UCL intensities. Under excitation of a 980 nm near-IR laser, the observed UCL intensities for the $BaYF_5$:Yb,Er,Bi_x UCNPs display first an increasing trend and then a decreasing trend with an increase in the ratio x, giving a maximum at x = 2.5. A possible energy-transfer process and simplified energy levels of the $BaYF_5$:Yb,Er,Bi_x UCNPs were proposed. The potential of the $BaYF_5$:Yb,Er,Bi_x UCNPs as contrast agents for computerized tomography (CT) imaging was successfully demonstrated. An obvious accumulation of $BaYF_5$:Yb,Er,Bi_x in tumor sites was achieved because of high passive targeting by the enhanced permeability and retention effect and relatively low uptake by a reticuloendothelial system such as liver and spleen. This work paves a new route for the design of luminescence-enhanced UNCPs as promising bioimaging agents for cancer theranostics.

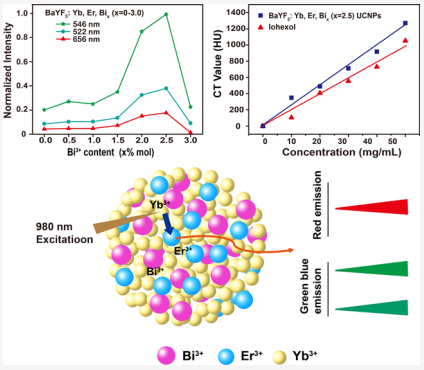

INTRODUCTION

Lanthanide ion (Ln^{3+})-doped upconversion nanoparticles (UCNPs) can absorb long-wavelength excitation and convert to short-wavelength emission via anti-Stokes processes, which have attracted extensive attention because their unique optical properties.[1−13] As a new generation of optical nanoprobes, UCNPs have been widely used in various fields such as clinical diagnosis and treatment as well as medical imaging research.[14−17] Among the various types of UCNPs, rare-earth fluoride compounds are considered to be the optimal host matrix for UCNPs because of their low phonon energy, superb light stability, and large anti-Stokes efficiency,[18−20] especially for the alkali-metal rare-earth fluorides and alkaline-earth-metal rare-earth fluorides.[8] As an important member of the rare-earth fluoride family, Ba^{2+}-containing rare-earth fluorides have been proven to be suitable matrixes for UCNPs.[3,8,18,19] Recently, Capobianco and his coauthors confirmed that Yb/Tm-codoped $BaYF_5$ has a brighter upconversion luminescence (UCL).[21] Lu and Liu's group also reported that the $BaYbF_5$ matrix not only owns excellent luminescence properties but also possesses strong X-ray computed tomography (CT) effects because of the large K-edge values and high X-ray mass absorption coefficients of the Ba and Yb elements.[22,23] Therefore, exploring Ba^{2+}-containing rare-earth fluoride UCNPs is of great significance for biomedical applications. However, the relatively low quantum efficiency is a common disadvantage of rare-earth fluoride UCNPs and greatly restricts their extensive and practical applications.

To date, many attempts have been made to enhance the UCL of the UCNPs for their biological applications such as bioimaging. Comparatively speaking, doping is a simple and effective strategy to modify the lattice and electronic structures of the phosphor host, thus significantly boosting their luminescence properties.[24−26] Two typical examples are that the UCL of the $NaLiYLuF_4$:Er,Yb microcrystals could be enhanced by doping Li^+ ions[24] and enhancement of the UCL in Zn_2SiO_4:Yb^{3+},Er^{3+} could be achieved by codoping Li^+ or Bi^{3+}.[26] As a unique alternative, Bi^{3+} is regarded as a viable non-rare-earth-element dopant for fluoride phosphors because of its special advantages, such as low toxicity, broad drug applications, and low cost.[27−30] What is more, a relatively broad emission and absorption band associated with the typical

Received: June 19, 2020

$6s^2 \rightarrow 6s6p$ transition make Bi^{3+} an excellent sensitizer to harvest the excitation light.[31−33] The previous researches have confirmed that Bi^{3+} can greatly sensitize the emission of lanthanides, especially for the UCL of Er^{3+} and Tm^{3+}, owing to an efficient energy transfer from Bi^{3+} to Ln^{3+}.[33] Actually, the doping of Bi^{3+} not only remarkably boosts the UCL intensity of the phosphor but also broadens its excitation band.[33] Predictably, the UCL intensity of the Ba^{2+}-containing rare-earth fluoride UCNPs also can be effectively enhanced via the introduction of Bi^{3+}.

CT imaging is widely used in medical diagnosis because of its ability to visualize the structure for living objects and provide exceptional three-dimensional (3D) anatomical information with different spatial resolutions according to the situation of the different organs and tissues.[34−37] Currently, the commonly used CT contrast agents with good X-ray absorption are mainly small iodinated molecules. However, these iodinated molecules suffer from short cycle life and potential renal toxicity. Therefore, the development of new CT contrast agents with low toxicity is very important and urgent. As is well-known, Ln^{3+}-doped UCNPs have low toxicity and good X-ray absorption, ensuring their use in CT imaging.[38−41] It is worth noting that Bi^{3+}-doped UCNPs may both possess excellent UCL and exhibit superior CT imaging ability. Especially, Yb^{3+},Er^{3+}-codoped $BaYF_5$ UCNPs possess large K-edge values and high X-ray mass absorption coefficients.[41−44] More importantly, the Bi element possesses a good X-ray attenuation property.[29] In general, the brighter the nanoprobe, the higher the signal-to-noise ratio that may be achieved in a biological imaging system. Because the above-mentioned characteristics of the Ba, Yb, and Bi elements can also synergistically integrate the merits of fluorescence and CT imaging while averting their individual demerits, making the Bi^{3+}-doped $BaYF_5$ UCNPs potential dual-modal fluorescence/CT imaging probes in single-phase materials. Unfortunately, there has not been any relevant research on the Bi^{3+}-doped $BaYF_5$ UCNPs and their biomedical applications until now.

Herein, $BaYF_5$:20%Yb^{3+}/2%Er^{3+}/x%Bi^{3+} (abbreviated as $BaYF_5$:Yb,Er,Bi_x, where x = 0−3.0) UCNPs were synthesized by a simple hydrothermal method. The influence of Bi^{3+} ions on the crystal phase, size, and upconversion (UC) emission of the obtained $BaYF_5$:Yb,Er,Bi_x UCNPs was investigated in detail. The green emission intensity for $BaYF_5$:Yb,Er,Bi_x (x = 2.5) UCNPs was 4 times greater than that of the Bi^{3+} free sample, and a longer decay time could be achieved through Bi^{3+} doping. Moreover, the citrate-functionalized $BaYF_5$:Yb,Er,Bi_x (x = 2.5) UCNPs for UCL and in vivo CT imaging were used out to investigate their biological applications. This work offers a new strategy for the design of luminescence-enhanced UCNPs and their biological applications.

■ EXPERIMENTAL SECTION

Materials. All chemicals including $Bi(NO_3)_3{\cdot}5H_2O$ (99%), $BaCl_2$ (98%), ethyl alcohol (95%), NH_4F (98%), trisodium citrate, Y_2O_3 (99.99%), Yb_2O_3 (99.9%), and Er_2O_3 (99.99%) were of analytical grade and were used as received without any further purification.

Preparation of $BaYF_5$:20%Yb^{3+}/2%Er^{3+}/x%Bi^{3+} (x = 0−3.0) UCNPs. In a typical synthesis procedure, Y_2O_3, Yb_2O_3, and Er_2O_3 were dissolved in 65% HNO_3 at 60 °C and stirred for 30 min to form pellucid solutions. The demand quantities of $Re(NO_3)_3$ (Re^{3+} = Y^{3+}, Yb^{3+}, and Er^{3+}), $Bi(NO_3)_3$, $BaCl_2$, and NH_4F solutions were obtained separately. Subsequently, 25 mL of a $BaCl_2$ solution was added into a 100 mL beaker and stirred for 30 min. According to the molar ratio of [$Re(NO_3)_3$ + $Bi(NO_3)_3$] to $BaCl_2$ of 1:1, the corresponding $Re(NO_3)_3$ and $Bi(NO_3)_3$ solutions were added into the beaker with continuous stirring for 0.5 h, and then 25 mmol of a NH_4F dilute solution was added dropwise into the above solution with vigorous stirring. Finally, the formed mixture was transferred into a 100 mL Teflon-lined autoclave and heated at 160 °C for 24 h. After that, the supernatant was discarded, and white precipitates were centrifuged three times in ethyl alcohol and three times in water. The collected precipitates were dried in air at 80 °C for 12 h.

Preparation of Citrate-Coated $BaYF_5$:20%Yb^{3+}/2%Er^{3+}/x% Bi^{3+}(x = 2.5) UCNPs. First, 100 mg of $BaYF_5$:Yb,Er,Bi_x (x = 2.5) UCNPs was added into 10 mL of a solution containing 300 mg of trisodium citrate under vigorous stirring for 4 h. Finally, the citrate-coated $BaYF_5$:Yb,Er,Bi_x (x = 2.5) UCNPs were washed with water and then separated by centrifugation.

Characterizations. X-ray diffraction (XRD) measurement (SmartLab, Cu Kα radiation) was used to confirm the crystal structures of the products. Fourier transform infrared (FT-IR) spectroscopy was recorded on an IR spectrophotometer (PerkinElmer 580B) using the KBr pellet technique. The elemental composition for the samples was determined by inductively coupled plasma mass spectrometry (ICP-MS; Aglient 8900). The morphology, size, and selected-area electron diffraction (SAED) pattern of the products were measured by transmission electron microscopy (TEM; FEI Tecani G2 F20). The size distribution of the samples was analyzed by ζ-potential measurements (Malvern Zetasizer NanoZS90). The absorption spectrum was measured using a PE Lambda 750 UV−vis−near-IR (NIR) spectrometer. The fluorescence spectrum was recorded using a fluorescence spectrophotometer (Hitachi F-7000) with a continuous 980 nm diode laser. The fluorescence decay curves were recorded on a fluorescence spectrophotometer (Edinburgh Instruments FLS1000).

Cytotoxicity Assay. The in vitro cytotoxicity experiment was done by the standard CCK-8 analysis method. Briefly, A549 cells were seeded into a 96-well cell culture plate at densities of 5×10^3 cells/well in Dulbecco's modified Eagle's medium (DMEM) containing 10% fetal bovine serum and a 1% penicillin−streptomycin solution at 37 °C in a humid atmosphere of 95% air and 5% CO_2 for 24 h. Then, different concentrations of citrate-coated $BaYF_5$:Yb,Er,Bi_x (x = 2.5) UCNPs (0, 15.63, 31.25, 62.50, 125, 250, and 500 μg/mL) were incubated with adherent A549 cells in 96-well plates for 24 h. Afterward, the culture medium was removed and then added with a serum-free DMEM-configured CCK-8 solution for 2 h. After centrifugation for 10 min, 80 μL of supernatant was sucked into another 96-well plate, and the absorbance at 452 nm was measured using the standard method.

In Vitro and in Vivo X-ray CT Imaging. To investigate whether the CT signal value was linear with the concentration of the $BaYF_5$:Yb,Er,Bi_x UCNPs, the in vitro CT imaging experiments were performed on a Quantum GX micro computed tomograph (PerkinElmer). The relevant detailed procedures and details are presented in the Supporting Information (SI). According to the standard protocol approved by the Key Laboratory for Biomedical Effects of Nanomaterials and Nanosafety (Institute of High Energy Physics, CAS), the mice were disposed of after the experiments were finished.[45]

■ RESULTS AND DISCUSSION

The phase structures of the obtained $BaYF_5$:20%Yb^{3+}/2%Er^{3+}/x%Bi^{3+} (x = 0−3.0) samples were determined by XRD. As disclosed in Figure 1a, all of the peaks can be well matched with the standard cubic $BaYF_5$ (ICSD 169849), implying that the as-prepared samples are pure cubic phases. Interestingly, compared with the standard cubic $BaYF_5$, the diffraction peaks of all of the $BaYF_5$:Yb,Er,Bi_x (x = 0−3.0) UCNPs slightly shift to the higher 2θ side because of the replacement of Y^{3+} (r = 1.159 Å) by a smaller Yb^{3+} (r = 1.125 Å).[29,46] Whereas the corresponding diffraction peaks of the $BaYF_5$:Yb,Er,Bi_x samples

https://dx.doi.org/10.1021/acs.inorgchem.0c01818
Inorg. Chem. XXXX, XXX, XXX−XXX

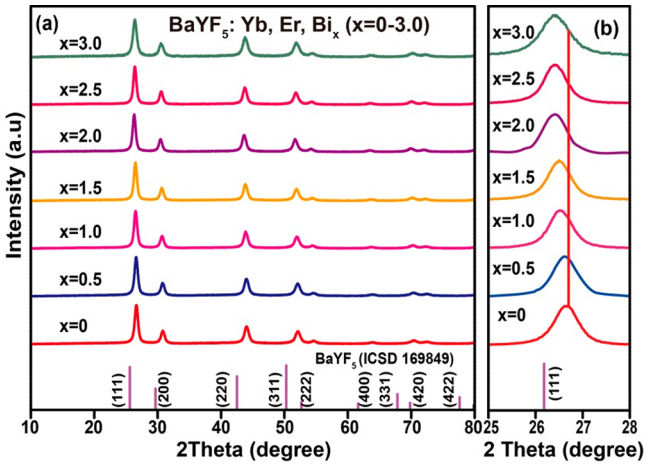

Figure 1. (a) XRD patterns of the $BaYF_5$:Yb,Er,Bi_x (x = 0−3.0) UCNPs. (b) Enlarged XRD patterns of the $BaYF_5$:Yb,Er,Bi_x (x = 0−3.0) UCNPs in the 2θ range from 25° to 28°.

shift to the lower 2θ side (Figure 1b), contrasting with the Bi^{3+}-free sample, this should be ascribed to replacement of the smaller Y^{3+} ions by the larger Bi^{3+} ions (r = 1.31 Å).[29,46] Moreover, the deviation degree in these diffraction peaks gradually increases with an ascending doping concentration of Bi^{3+}, suggesting that the Bi^{3+} ions were successfully incorporated into the $BaYF_5$ host lattice. Nevertheless, these results can also verify that the doping of a small amount of Bi^{3+} ions will not lead to variation of the phase structure for BYF_5:Yb,Er. To further verify these results, Rietveld refinements were also carried out. As shown in Figure S1, the refinement result of the representative $BaYF_5$:Yb,Er,Bi_x (x = 2.5%) sample is well consistent with that of the corresponding initial model with a reliability factor of χ^2 = 1.295, affirming that the obtained samples are in the cubic phase. To determine the suitable doping concentration of Bi^{3+} in the $BaYF_5$ host, we have synthesized the $BaYF_5$:Bi_x crystals (x = 1−7.0) and obtained their XRD patterns (Figure S2). It was found that the crucial doping concentration of Bi^{3+} for the $BaYF_5$ host was between 3 and 4%. It also can be seen that the obvious impure phase will appear as long as the doping concentration of Bi^{3+} exceeds 4%. Actually, 3% is the largest doping concentration of Bi^{3+} in the $BaYF_5$:Yb,Er,Bi_x UCNPs in our experimental conditions. What is more, the content of Bi^{3+} in the $BaYF_5$:Yb,Er,Bi_x (x = 0−3.0) samples was determined by ICP-MS, and the results are shown in Table S1. As shown in Table S1, the actual content of Bi^{3+} in the obtained $BaYF_5$:Yb,Er,Bi_x (x = 0−3.0) samples gradually ascends with the ascending concentration of Bi^{3+} in the starting solution. Nonetheless, the actual doping content of Bi^{3+} in the $BaYF_5$:Yb,Er,Bi_x (x = 0−3.0) samples is lower than the predetermined value, implying that some of the Bi^{3+} ions were left in the solution. Figure 2 shows the TEM images of the $BaYF_5$:Yb,Er,Bi_x (x = 0−3.0) UCNPs. It can be seen that all of the as-synthesized $BaYF_5$:Yb,Er,Bi_x samples are irregular nanoparticles with good dispersions, and the mean grain size is ∼20 nm. The high-resolution TEM (HR-TEM) image and SAED pattern of the representative $BaYF_5$:Yb,Er,Bi_x (x = 2.5%) UCNPs are also disclosed in Figure 2i,j, which clearly confirm the high crystalline nature of the as-prepared $BaYF_5$:Yb,Er,Bi_x (x = 2.5%) UCNPs. The measured distance between the adjacent lattice planes is 0.345 nm, which is well accordant with the d_{111} spacing of the cubic $BaYF_5$ (ICSD 169849). In addition, the SAED pattern in Figure 2j shows spotty polycrystalline diffraction rings corresponding to the (200), (220), and (311) planes of the cubic $BaYF_5$ lattice,

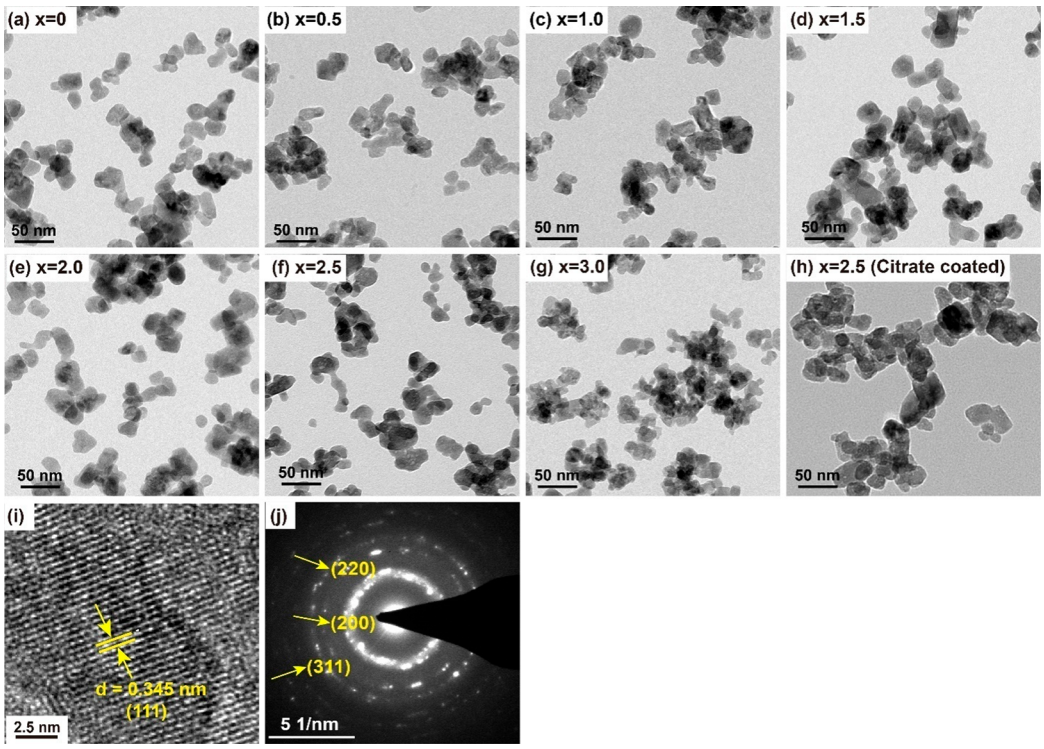

Figure 2. (a−h) TEM images of the $BaYF_5$:Yb,Er,Bi_x (x = 0−3.0) and citrate-coated $BaYF_5$:Yb,Er,Bi_x (x = 2.5) UCNPs, respectively. (i) HR-TEM image and (j) SAED pattern of the obtained $BaYF_5$:Yb,Er,Bi_x (x = 2.5) UCNPs.

https://dx.doi.org/10.1021/acs.inorgchem.0c01818
Inorg. Chem. XXXX, XXX, XXX−XXX

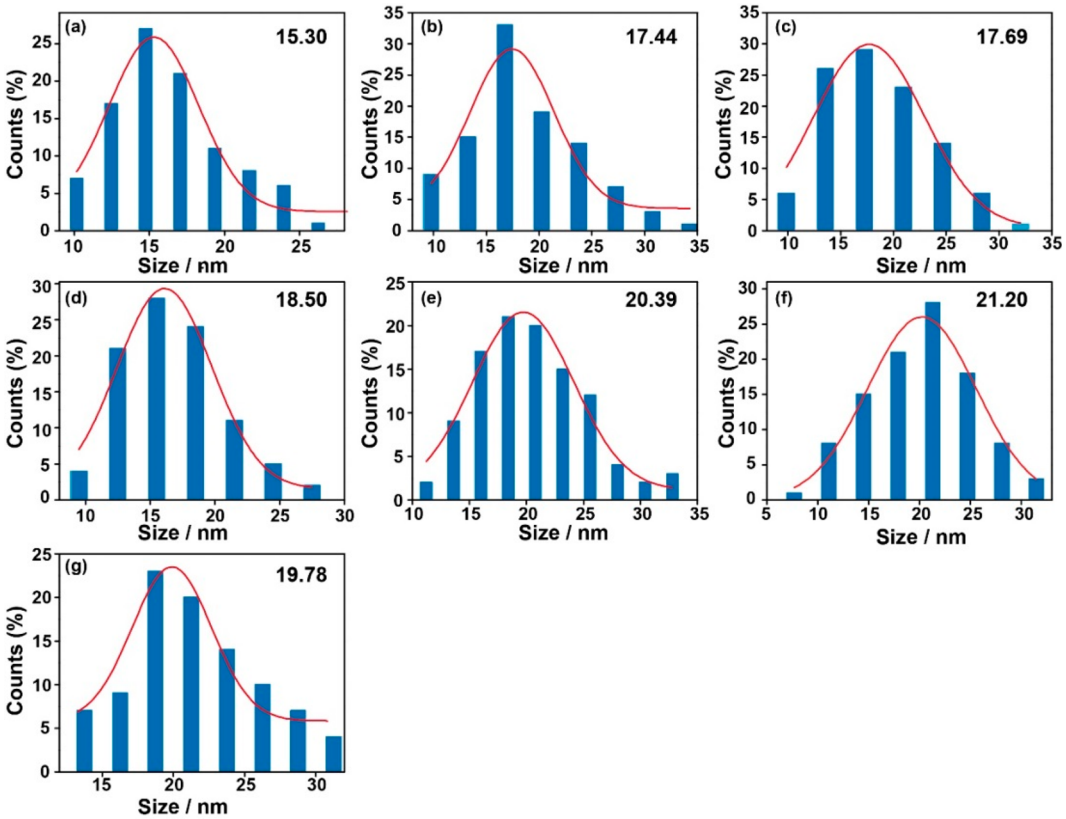

Figure 3. Size distribution of the $BaYF_5$:Yb,Er,Bi_x (x = 0−3.0) UCNPs: (a) x = 0; (b) x = 0.5; (c) x = 1.0; (d) x = 1.5; (e) x = 2.0; (f) x = 2.5; (g) x = 3.0.

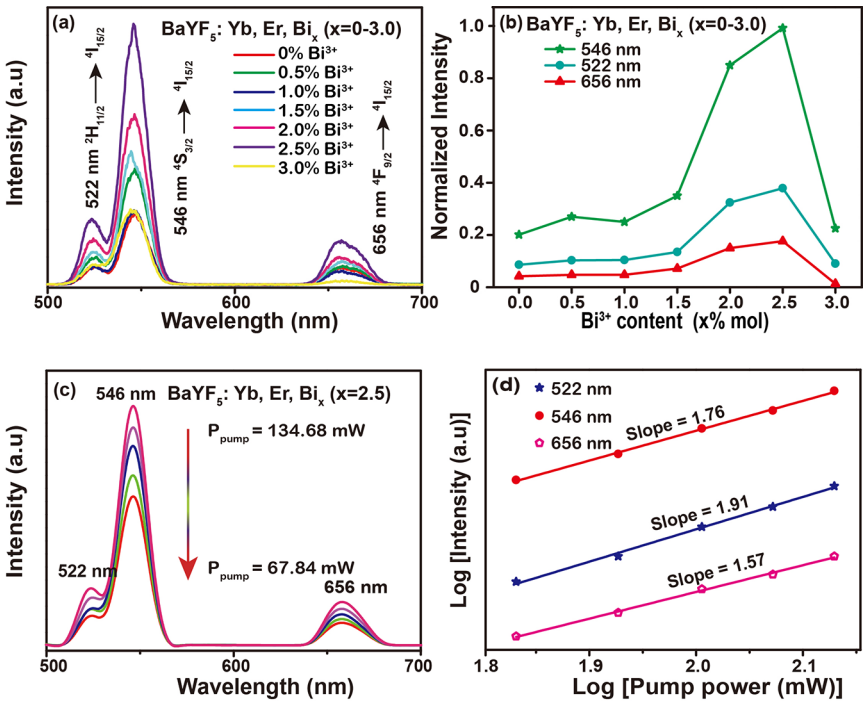

Figure 4. (a) UCL spectra of the $BaYF_5$:Yb,Er,Bi_x (x = 0−3.0) UCNPs under a 980 nm laser excitation. (b) Normalized UCL intensities of the green and red emissions for the $BaYF_5$:Yb,Er,Bi_x (x = 0−3.0) UCNPs. (c) Emission spectra of the $BaYF_5$:Yb,Er,Bi_x (x = 2.5) UCNPs pumped by a 980 nm laser with different powers (67.84, 84.55, 101.26, 117.97, and 134.68 mW). (d) Double logarithm of the upconversion emission intensity versus the pump power of the $BaYF_5$:Yb,Er,Bi_x (x = 2.5) UCNPs.

respectively, further confirming that the as-synthesized UCNPs possess a face-centered-cubic structure.

Figure 3 shows the size distribution of the prepared $BaYF_5$:Yb,Er,Bi_x (x = 0−3.0) UCNPs. With an increase of x,

https://dx.doi.org/10.1021/acs.inorgchem.0c01818
Inorg. Chem. XXXX, XXX, XXX−XXX

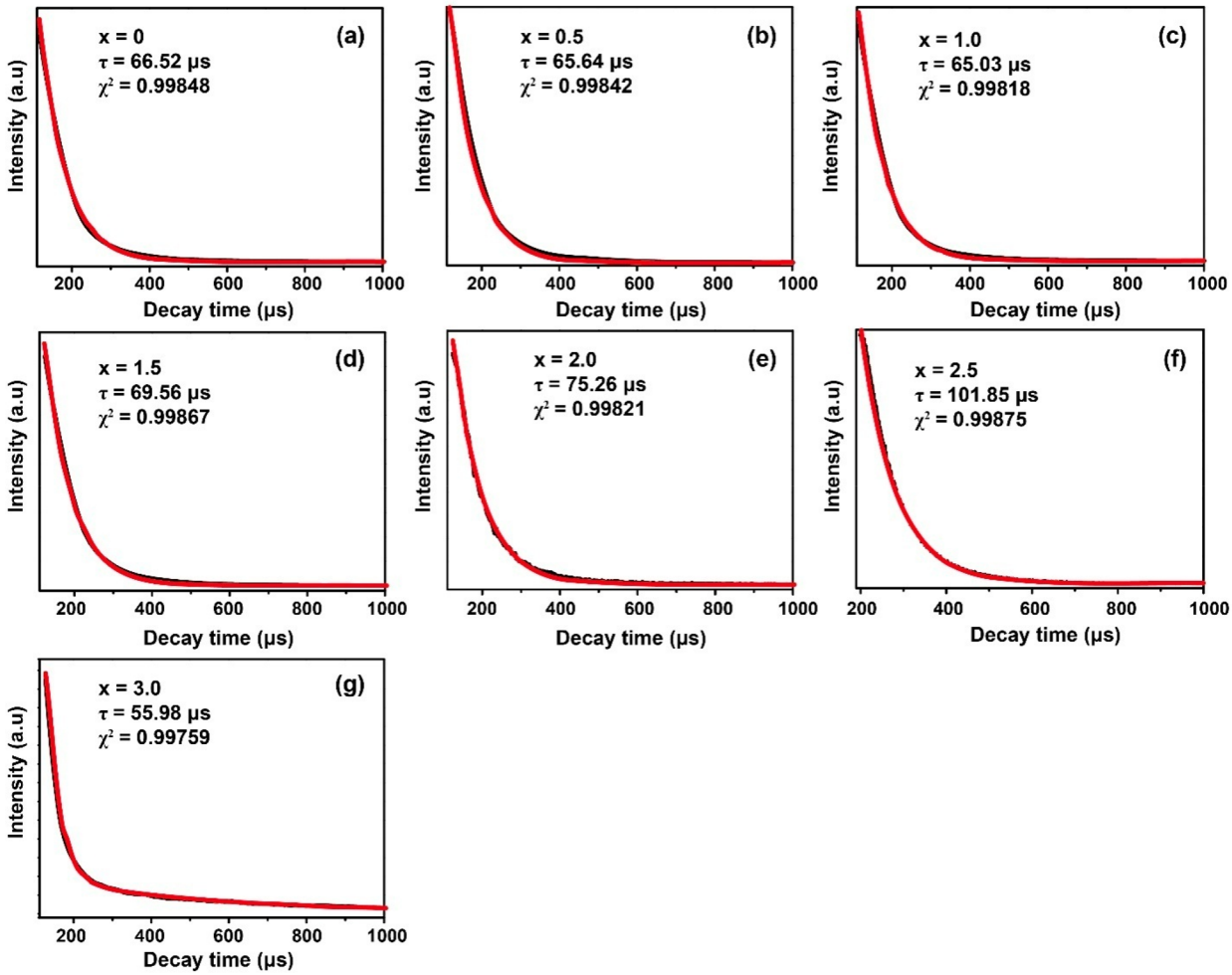

Figure 5. Decay curves for the $^4S_{3/2} \rightarrow {}^4I_{15/2}$ transition of Er^{3+} in the synthesized $BaYF_5$:Yb,Er,Bi_x (x = 0−3.0) UCNPs.

the particle size of the samples exhibits a slight increasing trend except for x = 3.0, and the average particle size for these samples is in the range of 15−21 nm. Similar results have been reported on the Bi^{3+}-doped $NaGdF_4$:Yb^{3+},Tm^{3+} UCNPs.[29] The comprehensive results of XRD, TEM, and ICP-MS indicate that Bi^{3+} was successfully incorporated into the $BaYF_5$ matrix, and the doping of Bi^{3+} has no significant effect on the microstructure of the samples. What deserves to be mentioned most is that all of the as-prepared $BaYF_5$:Yb,Er,Bi_x (x = 0−3.0) UCNPs possess smaller size and better uniformity, making them potential fluorescent probes for the biomedical applications.

The UV−vis−NIR absorption spectrum measured in the range of 200−900 nm for the $BaYF_5$:Yb,Er,Bi_x (x = 2.5) UCNPs is given in Figure S3. The observed absorption peaks of Er^{3+} and Bi^{3+} can well match with the corresponding excitation absorption peaks of Er^{3+} and Bi^{3+}, respectively. Detailed information is provided in the SI. The UCL spectra of the $BaYF_5$:Yb,Er,Bi_x (x = 0−3.0) UCNPs under 980 nm excitation are shown in Figure 4a. All of the samples present the main green emission peaks centered at 522 and 546 nm, respectively, derived from $^2H_{11/2} \rightarrow {}^4I_{15/2}$ and $^4S_{3/2} \rightarrow {}^4I_{15/2}$ transitions of Er^{3+} and a red emission centered at 656 nm originating from the $^4F_{9/2} \rightarrow {}^4I_{15/2}$ transition of Er^{3+}.[28,47,48] It should be noted that the concentration of Bi^{3+} has no obvious effect on the features of the emission peaks but significantly influences the UC intensities of the obtained $BaYF_5$:Yb,Er,Bi_x UCNPs. Figure 4b shows the normalized intensity of the two green emissions and one red emission as a function of the doping concentration of Bi^{3+} (i.e., x). With increasing concentration of Bi^{3+} from 0 to 3.0%, the UCL intensity initially increases and then decreases, showing the maximum at x = 2.5%. Especially, the emission intensities of the peaks located at 522, 546, and 656 nm for the $BaYF_5$:Yb,Er,Bi_x (x = 2.5) UCNPs are about 3, 4.3, and 4 times greater than those of the $BaYF_5$:Yb^{3+},Er^{3+} UCNPs, respectively. Indubitably, the doping moderate amount of Bi^{3+} ions can remarkably boost the green and red emissions of $BaYF_5$:Yb^{3+},Er^{3+} UCNPs.

Variation of the emission intensity for the obtained $BaYF_5$:Yb,Er,Bi_x (x = 0−3.0) UCNPs should be ascribed to the following aspects in our experiment. On the one hand, when the smaller Y^{3+} (r = 1.159 Å) is replaced by Bi^{3+} (r = 1.31 Å), the unit cell volume of the obtained nanocrystals will increase and the crystal-field symmetry around the Er^{3+} ion also will be changed, leading to a break of the forbidden transition around the Er^{3+} ion,[47] thus enhancing the UCL of the $BaYF_5$:Yb,Er,Bi_x UCNPs. On the other hand, the grain size of the samples also influences the UCL intensity because the relative intensity of the upconversion emission varies with the surface concentration quenching effect.[49,50] When $0 < x \leq 2.5\%$, the distortion degree of the crystal symmetry for the obtained $BaYF_5$:Yb,Er,Bi_x UCNPs gradually increases with the

https://dx.doi.org/10.1021/acs.inorgchem.0c01818
Inorg. Chem. XXXX, XXX, XXX−XXX

ascending doping concentration of Bi^{3+}, leading to the continuous increase of the UCL intensity accordingly. Simultaneously, the grain size of the $BaYF_5$:Yb,Er,Bi_x UCNPs slightly increases with the ascending x, also contributing to the enhancement of UCL intensity. Hence, the comprehensive effects of the above two aspects make the sample $BaYF_5$:Yb,Er,Bi_x with x = 2.5 exhibit the strongest UCL emission. As for the sample $BaYF_5$:Yb,Er,Bi_x with x = 3.0, the weakest UCL emission should be mainly attributed to the concentration quenching effect, although the reduced size also has some influence on the UCL emission. As mentioned earlier (see the SI), the crucial doping concentration of Bi^{3+} for the $BaYF_5$ host is between 3 and 4%, and it also can be seen that the obvious impure phase will appear as long as the doping concentration of Bi^{3+} exceeds 4%. Actually, 3% is the largest doping concentration of Bi^{3+} in the $BaYF_5$:Yb,Er,Bi_x UCNPs in our experimental conditions. For such a higher content of Bi^{3+} ions, Bi_n^{3+} aggregates may be formed, which play the role of trapping centers and consume the absorbed energy non-radiatively instead of transferring it to the Er^{3+} activator ions. Obviously, the probability of energy transfer from Bi^{3+} to Er^{3+} strongly relys on the doping concentration of Bi^{3+}. Similar results have been reported in the Er^{3+},Bi^{3+}-codoped $CaSnO_3$ nanocrystals and Eu^{3+},Bi^{3+}-codoped YVO_4 red phosphors.[51,52]

Figure 4c shows the UCL emission spectra of the $BaYF_5$:Yb,Er,Bi_x (x = 2.5) UCNPs pumped by a 980 nm laser with different powers. Under pumping of all of the powers, although the observed upconversion emission profiles for the $BaYF_5$:Yb,Er,Bi_x (x = 2.5) UCNPs are the same, the emission intensity increases with increasing power because of the boosted efficiency of UC multiple-step sensitizing energy transfer. To deeply investigate the involved UCL mechanism for the studied samples, the dependence of the green and red emission intensities of the $BaYF_5$:Yb,Er,Bi_x (x = 2.5) UCNPs on the pump power was measured, as disclosed in Figure 4d. The UCL emission intensity has a nonlinear dependence on the excitation power, which can be described by the following relationship:[47]

$$I \propto P^n \tag{1}$$

I represents the upconversion emission intensity, P represents the laser pump power, and n refers to the number of photons required in the UCL emission. The values of n for the UCL emissions centered at 522, 546, and 656 nm were deduced based on the double logarithm of the upconversion emission intensity versus the pump power of the $BaYF_5$:Yb,Er,Bi_x (x = 2.5) UCNPs. As shown in Figure 4d, the slopes of the linear fittings for the 522, 546, and 656 nm emissions are 1.91, 1.76, and 1.57, respectively, which indicate that a two-photon process is involved to produce the green and red emissions.

Figure 5 displays the decay curves for the $^4S_{3/2} \rightarrow {}^4I_{15/2}$ transition of Er^{3+} in the $BaYF_5$:Yb,Er,Bi_x (x = 0−3.0) UCNPs. These decay curves can be fitted to a single-exponential function as $I(t) = I_0 + A\exp(-t/\tau)$,[53] where A is constant, $I(t)$ and I_0 refer to the emission intensities at time t and 0, respectively, and τ represents the luminescence lifetime. As shown in Figure 5, the decay times of these $BaYF_5$:Yb,Er,Bi_x samples were determined to be 66.52, 65.64, 65.03, 69.56, 75.26, 101.85, and 55.98 μs, respectively, and basically match with their UCL emission intensities. Obviously, the luminescence lifetimes of the $BaYF_5$:Yb,Er UCNPs can be markedly prolonged after doping a suitable amount of Bi^{3+} ions, effectively enhancing their UCL. Accordingly, the improvement mechanism in the luminescence lifetime is similar to their enhancement in UCL. In other words, it should be attributed to the synergistic effect of the symmetric distortion around the Er^{3+} crystal field and grain-size-induced surface concentration quenching effect. On the basis of the reported energy transfer in Bi^{3+},Er^{3+}-codoped phosphors[33] and the existing energy transfer in Yb^{3+},Er^{3+}-codoped fluoride systems,[19,34,41] a possible energy-transfer process and simplified energy levels of the $BaYF_5$:Yb,Er,Bi_x (x = 0−3.0) UCNPs are shown in Figure 6. Detailed explanations are shown in the SI.

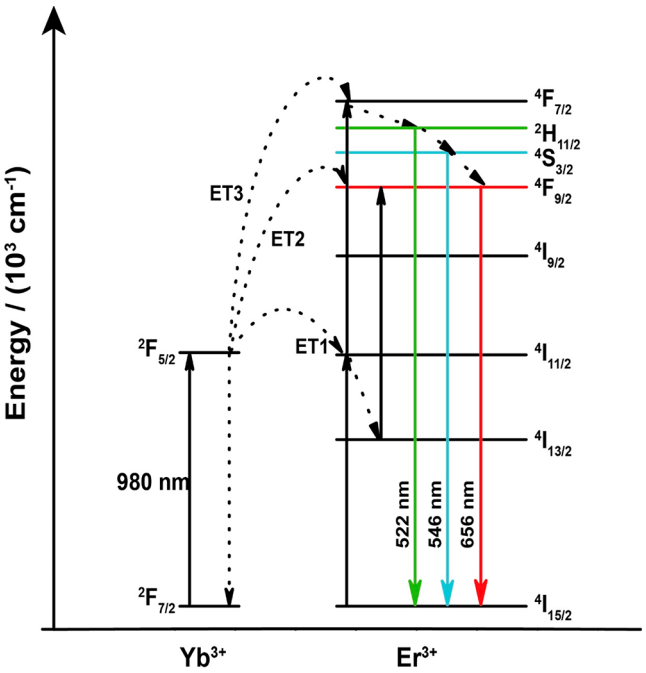

Figure 6. Schematic diagram of the energy-level structure of the $BaYF_5$:Yb,Er,Bi_x UCNPs.

For the subsequent biological experiment, the selected $BaYF_5$:Yb,Er,Bi_x (x = 2.5) UCNPs were modified with citrate, and the successful surface modification of citrate was verified by FT-IR spectroscopy (Figure S4). The cytotoxicity test was carried out on human lungadenocarcinoma cancer cells (A549) through the standard CCK-8 assay. After incubation with the citrate-coated $BaYF_5$:Yb,Er,Bi_x (x = 2.5) UCNPs at different concentrations (15.63−500 μg/mL) for 24 h, the cell viability of A549 was still maintained at a high level (Figure S5). Even after the concentration of the UCNPs increased to 500 μg/mL, the cell viability can still maintain about 87%, suggesting that the $BaYF_5$:Yb,Er,Bi_x (x = 2.5) UCNPs have negligible cell toxicity and can be safely used for bioimaging.

X-ray CT imaging is widely used as a reliable clinical diagnosis because of the high-resolution 3D structure details and deep penetration.[34−37] First, we compared the CT imaging capability in vitro for all of the obtained $BaYF_5$:Yb,Er,Bi_x (x = 0−3.0) UCNPs, and the results and corresponding explanations are provided (Figure S6 and Table S2). It can be seen that the doping concentration of Bi^{3+} has a very weak influence on the CT signal of these $BaYF_5$:Yb,Er,Bi_x (x = 0−3.0) UCNPs, which could be attributed to the much lower doping level of Bi^{3+}. In view of the strongest UCL emission, we therefore compared the CT imaging signal of the citrate-coated $BaYF_5$:Yb,Er,Bi_x (x = 2.5) UCNPs with that of the

https://dx.doi.org/10.1021/acs.inorgchem.0c01818
Inorg. Chem. XXXX, XXX, XXX−XXX

commercially used iohexol in vitro. With an increase of the concentration from 0 to 50 mg/mL, the CT contrast signals of the citrate-coated $BaYF_5$:Yb,Er,Bi_x (x = 2.5) UCNPs and iohexol obviously enhanced (Figure 7a). A good linear

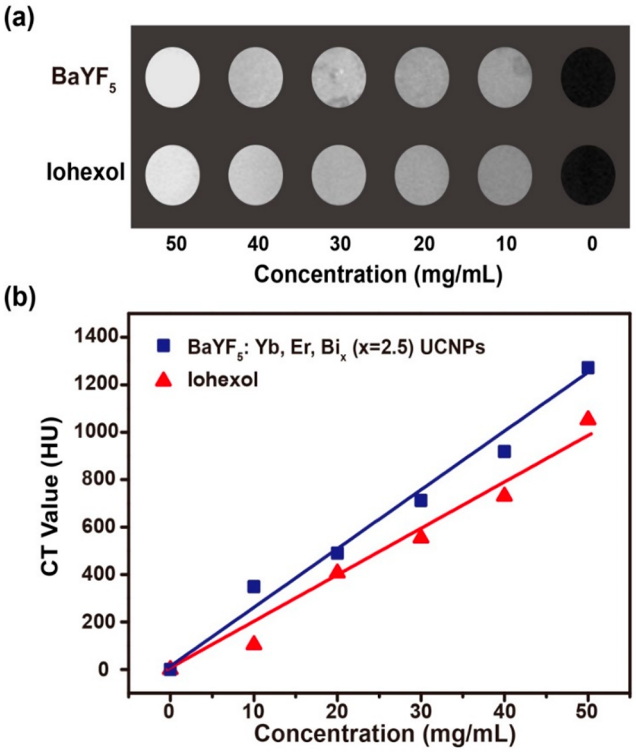

Figure 7. (a) In vitro CT images of the citrate-coated $BaYF_5$:Yb,Er,Bi_x (x = 2.5) UCNPs and iohexol at different concentrations. (b) CT value (HU) of the citrate-coated $BaYF_5$:Yb,Er,Bi_x (x = 2.5) UCNPs and iohexol as a function of the concentrations of the citrate-coated $BaYF_5$:Yb,Er,Bi_x (x = 2.5) UCNPs and iohexol, respectively.

relationship between the Hounsfield units (HU) value and concentrations of both the $BaYF_5$:Yb,Er,Bi_x (x = 2.5) UCNPs and iohexol can be observed (Figure 7b). Evidently, the HU values of the citrate-coated $BaYF_5$:Yb,Er,Bi_x (x = 2.5) UCNPs are higher than that of iohexol at equivalent concentrations, confirming that the obtained UCNPs are efficient contrast agents for CT imaging. The good CT imaging performance of the $BaYF_5$:Yb,Er,Bi_x (x = 2.5) UCNPs in vitro motivated us to further use $BaYF_5$:Yb,Er,Bi_x (x = 2.5) for in vivo CT imaging. As shown in Figure 8, the tumor CT images were obtained preinjection (0 h) and after intratumoral injection of the citrate-coated $BaYF_5$:Yb,Er,Bi_x (x = 2.5) UCNPs at different time intervals for 2, 8, and 12 h. The bright-field image of the mouse before intratumoral injection of the citrate-coated $BaYF_5$:Yb,Er,Bi_x (x = 2.5) UCNPs was recorded in Figure S7. The tumor site shows an obvious enhancement with a significantly higher CT value 8−12 h postinjection, as shown in Figure 8c,d, which is also evidence for the high accumulation in tumor sites. Moreover, Figure S8 also gives the signal intensities in the tumor obtained preinjection (0 h) and after intratumoral injection of the citrate-coated $BaYF_5$:Yb,Er,Bi_x (x = 2.5) UCNPs at different time intervals. Apparently, the time-dependent accumulation of $BaYF_5$:Yb,Er,Bi_x in tumor sites was observed within 12 h. The obvious accumulation of $BaYF_5$:Yb,Er,Bi_x in tumor sites along with negligible uptake in a reticuloendothelial system (RES)

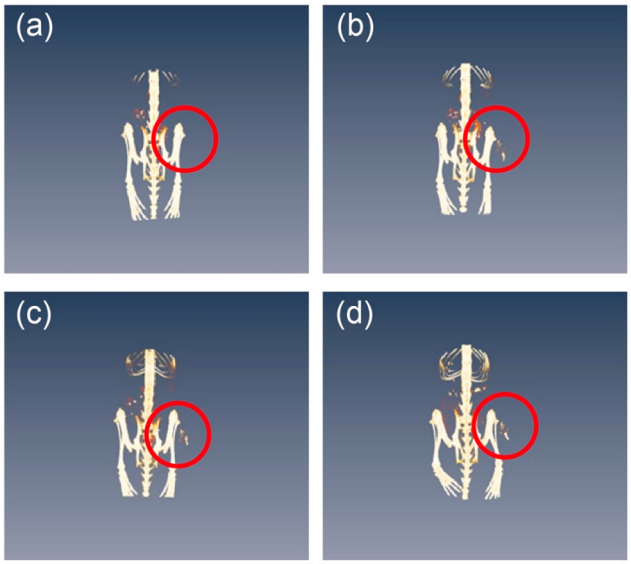

Figure 8. In vivo CT images of the mice after intratumoral injection of the citrate-coated $BaYF_5$:Yb,Er,Bi_x (x = 2.5) UCNPs: (a) preinjection; (b) 2, (c) 8, and (d) 12 h postinjection.

such as liver and spleen could be attributed to high passive targeting by the enhanced permeability and retention effect (EPR) and relatively low uptake by the RES. In addition, we calculated the X-ray absorption coefficients of the $BaYF_5$:Yb,Er,Bi_x UCNPs by the *XMuDat* computer program, and the obtained X-ray absorption coefficients of the $BaYF_5$:Yb,Er,Bi_x UCNPs as a function of the photon energy have also been provided.[54] All of the samples have very similar relationship graphs of the X-ray absorption coefficients as a function of the photon energy, and they almost overlapped; hence, we just display the curve for the representative sample of the $BaYF_5$:Yb,Er,Bi_x UCNPs (x = 2.5; Figure S9). It can be seen that the obtained attenuation coefficient of the $BaYF_5$:Yb,Er,Bi_x UCNPs (x = 2.5) is comparable to those of other high-Z nanomaterials such as Bi_2S_3, Bi_2Se_3, and Cu_3BiS_3 and is rather higher than that of the soft tissues, suggesting that these $BaYF_5$:Yb,Er,Bi_x UCNPs are capable of concentrating more X-ray dose into tumor tissues for enhanced CT imaging and even great potential for radiotherapy in the future.[54]

■ CONCLUSIONS

In summary, we have successfully synthesized a series of the $BaYF_5$:Yb,Er,Bi_x (x = 0−3.0) UCNPs by a facile hydrothermal method. Although the doping concentration of Bi^{3+} has negligible influence on the microstructures of the $BaYF_5$:Yb,Er,Bi_x UCNPs, it remarkably affects their UCL intensities. The $BaYF_5$:Yb,Er,Bi_x (x = 2.5) UCNPs own the strongest green emission intensity, exhibiting about 3−4 times enhancement compared with that of the Bi^{3+} free sample. A possible energy-transfer process and simplified energy levels of the $BaYF_5$:Yb,Er,Bi_x UCNPs were also proposed. Compared with iohexol, the as-synthesized $BaYF_5$:Yb,Er,Bi_x (x = 2.5) UCNPs possess significant CT signals, showing potential biomedical applications as an ideal CT imaging contrast agent. The obvious accumulation of $BaYF_5$:Yb,Er,Bi_x in tumor sites was observed during in vivo CT imaging. It was suggested that the citrate-coated $BaYF_5$:Yb,Er,Bi_x (x = 2.5) UCNPs have a high EPR effect and relatively low uptake by the RES. This work provides a new strategy for the design of luminescence-

https://dx.doi.org/10.1021/acs.inorgchem.0c01818
Inorg. Chem. XXXX, XXX, XXX−XXX

enhanced UNCPs as a promising cancer nanotheranostic for bioimaging and cancer treatment.

■ ASSOCIATED CONTENT

Supporting Information

The Supporting Information is available free of charge at https://pubs.acs.org/doi/10.1021/acs.inorgchem.0c01818.

Rietveld XRD refinement of the $BaYF_5$:Yb,Er,Bi_x (x = 2.5) UCNPs, ICP-MS of the $BaYF_5$:Yb,Er,Bi_x (x = 0−3.0) UCNPs, FT-IR spectra of the $BaYF_5$:Yb,Er,Bi_x (x = 2.5) and citrate-coated $BaYF_5$:Yb,Er,Bi_x (x = 2.5) UCNPs, viability of A549 cells incubated with the citrate-coated $BaYF_5$:Yb,Er,Bi_x (x = 2.5) UCNPs (15.63−1000 μg/mL) for 24 h by the standard CCK-8 assay and bright-field image of the mouse before intratumoral injection of the citrate-coated $BaYF_5$:Yb,Er,Bi_x (x = 2.5) UCNPs, in vitro and in vivo X-ray CT imaging and a possible energy-transfer process in the $BaYF_5$:Yb,Er,Bi_x UCNPs, and X-ray absorption coefficients of the $BaYF_5$:Yb,Er,Bi_x (x = 2.5) UCNPs as a function of the photon energy (PDF)

■ AUTHOR INFORMATION

Corresponding Authors

Yan Zhao − *College of Chemistry and Materials Science, Sichuan Normal University, Chengdu 610066, P. R. China;* orcid.org/0000-0001-6318-6082; Email: zhaoyan@sicnu.edu.cn

Wenyan Yin − *Key Laboratory for Biomedical Effects of Nanomaterials and Nanosafety, Institute of High Energy Physics, Chinese Academy of Sciences (CAS), Beijing 100049, P. R. China; CAS Key Laboratory of Nano-Bio Interface, Suzhou Institute of Nano-Tech and Nano-Bionics, Chinese Academy of Sciences (CAS), Suzhou 215123, P. R. China;* orcid.org/0000-0001-6726-3938; Email: yinwy@ihep.ac.cn

Daojiang Gao − *College of Chemistry and Materials Science, Sichuan Normal University, Chengdu 610066, P. R. China;* orcid.org/0000-0003-3600-9712; Email: daojianggao@sicnu.edu.cn, daojianggao@126.com

Authors

Ran Luo − *College of Chemistry and Materials Science, Sichuan Normal University, Chengdu 610066, P. R. China*

Lei Chen − *Key Laboratory for Biomedical Effects of Nanomaterials and Nanosafety, Institute of High Energy Physics, Chinese Academy of Sciences (CAS), Beijing 100049, P. R. China;* orcid.org/0000-0002-8148-2982

Qinyu Li − *College of Chemistry and Materials Science, Sichuan Normal University, Chengdu 610066, P. R. China*

Jie Zhou − *Key Laboratory for Biomedical Effects of Nanomaterials and Nanosafety, Institute of High Energy Physics, Chinese Academy of Sciences (CAS), Beijing 100049, P. R. China*

Linqiang Mei − *Key Laboratory for Biomedical Effects of Nanomaterials and Nanosafety, Institute of High Energy Physics, Chinese Academy of Sciences (CAS), Beijing 100049, P. R. China*

Zhanglei Ning − *College of Chemistry and Materials Science, Sichuan Normal University, Chengdu 610066, P. R. China;* orcid.org/0000-0001-5580-0708

Mengjiao Liu − *College of Chemistry and Materials Science, Sichuan Normal University, Chengdu 610066, P. R. China*

Xin Lai − *College of Chemistry and Materials Science, Sichuan Normal University, Chengdu 610066, P. R. China*

Jian Bi − *College of Chemistry and Materials Science, Sichuan Normal University, Chengdu 610066, P. R. China*

Complete contact information is available at: https://pubs.acs.org/10.1021/acs.inorgchem.0c01818

Author Contributions

The manuscript was written through contributions of all authors. All authors have given approval to the final version of the manuscript.

Notes

The authors declare no competing financial interest.

■ ACKNOWLEDGMENTS

This work was supported by the Sichuan Science and Technology Program (Grant 2019YJ0525), Scientific Research Fund of Sichuan Provincial Education Department of Sichuan Province (Grant 16TD0007), National Basic Research Programs of China (Grant 2016YFA0201600), National Natural Science Foundation of China (Grants 51772293 and U1932112), Beijing Natural Science Foundation (Grant 2202064), and CAS Key Laboratory of Nano-Bio Interface (Grant 20NBI01).

■ REFERENCES

(1) Na, H.; Jeong, J. S.; Chang, H. J.; Kim, H. Y.; Woo, K.; Lim, K.; Mkhoyan, K. A.; Jang, H. S. Facile synthesis of intense green-emitting $LiGdF_4$: Yb, Er-based upconversion bipyramidal nanocrystals and their polymer composites. *Nanoscale* **2014**, *6*, 7461−7468.

(2) Huang, Y.; You, H.; Jia, G.; Song, Y.; Zheng, Y.; Yang, M.; Liu, K.; Guo, N. Hydrothermal synthesis, cubic structure, and luminescence properties of $BaYF_5$: RE (RE = Eu, Ce, Tb) nanocrystals. *J. Phys. Chem. C* **2010**, *114*, 18051−18058.

(3) Grzyb, T.; Przybylska, D. Formation mechanism, structural, and upconversion properties of alkaline rare-earth fluoride nanocrystals doped with Yb^{3+}/Er^{3+} ions. *Inorg. Chem.* **2018**, *57*, 6410−6420.

(4) Kore, B. P.; Kumar, A.; Erasmus, L.; Kroon, R. E.; Terblans, J. J.; Dhoble, S. J.; Swart, H. C. Energy transfer mechanisms and optical thermometry of $BaMgF_4$:Yb^{3+}, Er^{3+} phosphor. *Inorg. Chem.* **2018**, *57*, 288−299.

(5) Zhou, J.; Liu, Q.; Feng, W.; Sun, Y.; Li, F. Upconversion luminescent materials: advances and applications. *Chem. Rev.* **2015**, *115*, 395−465.

(6) Wang, X.; Li, Y. Monodisperse nanocrystals: general synthesis, assembly, and their applications. *Chem. Commun.* **2007**, *28*, 2901−2910.

(7) Wu, Y.; Ji, Y.; Xu, J.; Liu, J.; Lin, Z.; Zhao, Y.; Sun, Y.; Xu, L.; Chen, K. Crystalline phase and morphology controlling to enhance the up-conversion emission from $NaYF_4$:Yb, Er nanocrystals. *Acta Mater.* **2017**, *131*, 373−379.

(8) Li, T.; Li, Y.; Luo, R.; Ning, Z.; Zhao, Y.; Liu, M.; Lai, X.; Zhong, C.; Wang, C.; Zhang, J.; Bi, J.; Gao, D. Novel $Ba(Gd_{1-x}Y_x)_{0.78}F_5$: 20 mol% Yb^{3+}, 2 mol% Tm^{3+} ($0 \leq x \leq 1.0$) solid solution nanocrystals: A facile hydrothermal controlled synthesis, enhanced upconversion luminescent and paramagnetic properties. *J. Alloys Compd.* **2018**, *740*, 1204−1214.

(9) Luo, R.; Li, T.; Chen, Y.; Ning, Z.; Zhao, Y.; Liu, M.; Lai, X.; Zhong, C.; Wang, C.; Bi, J.; Gao, D. $Na_{(1-x)}Li_x(Gd_{0.39}Y_{0.39}Yb_{0.2}Er_{0.02})F_4$ ($0 \leq x \leq 1$) solid solution microcrystals: Li/Na ratio-induced transition of crystalline phase and morphology, and their enhanced upconversion emission. *Cryst. Growth Des.* **2018**, *18*, 6581−6590.

(10) Zheng, W.; Huang, P.; Tu, D.; Ma, E.; Zhu, H.; Chen, X. Lanthanide-doped upconversion nano-bioprobes: electronic structures, optical properties, and biodetection. *Chem. Soc. Rev.* **2015**, *44*, 1379−1415.

(11) Zhou, L.; Wang, R.; Yao, C.; Li, X.; Wang, C.; Zhang, X.; Xu, C.; Zeng, A.; Zhao, D.; Zhang, F. Single-band upconversion nanoprobes for multiplexed simultaneous in situ molecularmapping of cancer biomarkers. *Nat. Commun.* **2015**, *6*, 6938.

(12) Fan, Y.; Wang, P.; Lu, Y.; Wang, R.; Zhou, L.; Zheng, X.; Li, X.; Piper, J. A.; Zhang, F. Lifetime-engineered NIR-II nanoparticles unlock multiplexed in vivo imaging. *Nat. Nanotechnol.* **2018**, *13*, 941−946.

(13) Zhang, H.; Fan, Y.; Pei, P.; Sun, C.; Lu, L.; Zhang, F. Tm^{3+}-sensitized NIR-II fluorescent nanocrystals for in vivo information storage and decoding. *Angew. Chem., Int. Ed.* **2019**, *58*, 10153−10157.

(14) An, R.; Lei, P.; Zhang, P.; Xu, X.; Feng, J.; Zhang, H. Near-infrared optical and X-ray computed tomography dual-modal imaging probe based on novel lanthanide-doped $K_{0.3}Bi_{0.7}F_{2.4}$ upconversion nanoparticles. *Nanoscale* **2018**, *10*, 1394−1402.

(15) Xia, A.; Deng, Y.; Shi, H.; Hu, J.; Zhang, J.; Wu, S.; Chen, Q.; Huang, X.; Shen, J. Polypeptide-functionalized $NaYF_4$:Yb^{3+}, Er^{3+} nanoparticles: red-emission biomarkers for high quality bioimaging using a 915 nm laser. *ACS Appl. Mater. Interfaces* **2014**, *6*, 18329−18336.

(16) Li, Z.; Lv, S.; Wang, Y.; Chen, S.; Liu, Z. Construction of LRET-based nanoprobe using upconversion nanoparticles with confined emitters and bared surface as luminophore. *J. Am. Chem. Soc.* **2015**, *137*, 3421−3427.

(17) Ma, D.; Meng, L.; Chen, Y.; Hu, M.; Chen, Y.; Huang, C.; Shang, J.; Wang, R.; Guo, Y.; Yang, J. $NaGdF_4$:Yb^{3+}/Er^{3+}@$NaGdF_4$:Nd^{3+}@sodium-gluconate: multifunctional and biocompatible ultrasmall core-shell nanohybrids for UCL/MR/CT multimodal imaging. *ACS Appl. Mater. Interfaces* **2015**, *7*, 16257−16265.

(18) Li, X.; Zhang, F.; Zhao, D. Lab on upconversion nanoparticles: optical properties and applications engineering via designed nanostructure. *Chem. Soc. Rev.* **2015**, *44*, 1346−1378.

(19) Zhang, C.; Ma, P.; Li, C.; Li, G.; Huang, S.; Yang, D.; Shang, M.; Kang, X.; Lin, J. Controllable and white upconversion luminescence in $BaYF_5$:Ln^{3+} (Ln = Yb, Er, Tm) nanocrystals. *J. Mater. Chem.* **2011**, *21*, 717−723.

(20) Yi, Z.; Li, X.; Xue, Z.; Liang, X.; Lu, W.; Peng, H.; Liu, H.; Zeng, S.; Hao, J. Remarkable NIR enhancement of multifunctional nanoprobes for *in vivo* trimodal bioimaging and upconversion optical/T_2 -weighted MRI-guided small tumor diagnosis. *Adv. Funct. Mater.* **2015**, *25*, 7119−7129.

(21) Vetrone, F.; Mahalingam, V.; Capobianco, J. A. Near-infrared-to-blue upconversion in colloidal $BaYF_5$:Tm^{3+}, Yb^{3+} nanocrystals. *Chem. Mater.* **2009**, *21*, 1847−1851.

(22) Liu, Y.; Ai, K.; Liu, J.; Yuan, Q.; He, Y.; Lu, L. Hybrid $BaYbF_5$ nanoparticles: novel binary contrast agent for high-resolution *in vivo* X-ray computed tomography angiography. *Adv. Healthcare Mater.* **2012**, *1*, 461−466.

(23) Li, X.; Yi, Z.; Xue, Z.; Zeng, S.; Liu, H. Multifunctional $BaYbF_5$: Gd/Er upconversion nanoparticles for *in vivo* tri-modal upconversion optical, X-ray computed tomography and magnetic resonance imaging. *Mater. Sci. Eng., C* **2017**, *75*, 510−516.

(24) Ju, D.; Song, F.; Han, Y.; Cui, W.; Song, F.; Liu, L.; Zhou, A.; Wang, X.; Liu, S. Morphology control and upconversion luminescence enhancement of $Na_{1-x}Li_xY_{.78-y}Lu_yF_4$:$Er_{.02}Yb_{.2}$ microcrystals by doping ions with different valences. *J. Lumin.* **2018**, *198*, 46−53.

(25) Bhargavi, K.; Sundara Rao, M.; Sudarsan, V.; Srinivasa Rao, C.; Piasecki, M.; Kityk, I. V.; Srinivasa Reddy, M.; Veeraiah, N. Influence of Al^{3+} ions on self up-conversion in Ho^{3+} doped lead silicate glasses. *Opt. Mater.* **2014**, *36*, 1189−1196.

(26) Jiang, L.; Xiao, S.; Yang, X.; Ding, J.; Dong, K. Enhancement of up-conversion luminescence in Zn_2SiO_4:Yb^{3+}, Er^{3+} by co-doping with Li^+ or Bi^{3+}. *Appl. Phys. B: Lasers Opt.* **2012**, *107*, 477−481.

(27) Du, P.; Huang, X.; Yu, J. S. Facile synthesis of bifunctional Eu^{3+}-activated $NaBiF_4$ red-emitting nanoparticles for simultaneous white light-emitting diodes and field emission displays. *Chem. Eng. J.* **2018**, *337*, 91−100.

(28) Huang, X.; Jiang, L.; Xu, Q.; Li, X.; He, A. Low-temperature molten-salt synthesis and upconversion of novel hexagonal $NaBiF_4$: Er^{3+} /Yb^{3+} micro-/nanocrystals. *RSC Adv.* **2017**, *7*, 41190−41203.

(29) Lei, P.; Zhang, P.; Yao, S.; Song, S.; Dong, L.; Xu, X.; Liu, X.; Du, K.; Feng, J.; Zhang, H. Optimization of Bi^{3+} in upconversion nanoparticles induced simultaneous enhancement of near-infrared optical and X-ray computed tomography imaging capability. *ACS Appl. Mater. Interfaces* **2016**, *8*, 27490−27497.

(30) Lei, P.; An, R.; Yao, S.; Wang, Q.; Dong, L.; Xu, X.; Du, K.; Feng, J.; Zhang, H. Ultrafast synthesis of novel hexagonal phase $NaBiF_4$ upconversion nanoparticles at room temperature. *Adv. Mater.* **2017**, *29*, 1700505.

(31) Wang, L. L.; Wang, Q. L.; Xu, X. Y.; Li, J. Z.; Gao, L. B.; Kang, W. K.; Shi, J. S.; Wang, J. Energy transfer from Bi^{3+} to Eu^{3+} triggers exceptional long-wavelength excitation band in $ZnWO_4$:Bi^{3+}, Eu^{3+} phosphors. *J. Mater. Chem. C* **2013**, *1*, 8033−8040.

(32) Awater, R. H. P.; Dorenbos, P. Towards a general concentration quenching model of Bi^{3+} luminescence. *J. Lumin.* **2017**, *188*, 487−489.

(33) Xue, J.; Wang, X.; Jeong, J. H.; Yan, X. Spectral and energy transfer in Bi^{3+}-Re^{n+} (n = 2, 3, 4) co-doped phosphors: extended optical applications. *Phys. Chem. Chem. Phys.* **2018**, *20*, 11516−11541.

(34) Liu, H.; Lu, W.; Wang, H.; Rao, L.; Yi, Z.; Zeng, S.; Hao, J. Simultaneous synthesis and amine-functionalization of single-phase $BaYF_5$:Yb/Er nanoprobe for dual-modal *in vivo* upconversion fluorescence and long-lasting X-ray computed tomography imaging. *Nanoscale* **2013**, *5*, 6023−6029.

(35) Chen, G.; Qiu, H.; Prasad, P. N.; Chen, X. Upconversion nanoparticles: design, nanochemistry, and applications in theranostics. *Chem. Rev.* **2014**, *114*, 5161−5214.

(36) Zhang, W.; Shen, Y.; Liu, M.; Gao, P.; Pu, H.; Fan, L.; Jiang, R.; Liu, Z.; Shi, F.; Lu, H. Sub-10 nm water-dispersible β-$NaGdF_4$:x% Eu^{3+} nanoparticles with enhanced biocompatibility for *in vivo* X-ray luminescence computed tomography. *ACS Appl. Mater. Interfaces* **2017**, *9*, 39985−39993.

(37) Lv, R.; Yang, P.; He, F.; Gai, S.; Li, C.; Dai, Y.; Yang, G.; Lin, J. A yolk-like multifunctional platform for multimodal imaging and synergistic therapy triggered by a single near-infrared light. *ACS Nano* **2015**, *9*, 1630−1647.

(38) Kumar, R.; Nyk, M.; Ohulchanskyy, T. Y.; Flask, C. A.; Prasad, P. N. Combined optical and MR bioimaging using rare earth ion doped $NaYF_4$ nanocrystals. *Adv. Funct. Mater.* **2009**, *19*, 853−859.

(39) Zhou, J.; Sun, Y.; Du, X.; Xiong, L.; Hu, H.; Li, F. Dual-modality *in vivo* imaging using rare-earth nanocrystals with near-infrared to near-infrared (NIR-to-NIR) upconversion luminescence and magnetic resonance properties. *Biomaterials* **2010**, *31*, 3287−3295.

(40) Ramasamy, P.; Chandra, P.; Rhee, S. W.; Kim, J. Enhanced upconversion luminescence in $NaGdF_4$:Yb, Er nanocrystals by Fe^{3+} doping and their application in bioimaging. *Nanoscale* **2013**, *5*, 8711−8717.

(41) Runowski, M.; Stopikowska, N.; Szeremeta, D.; Goderski, S.; Skwierczyńska, M.; Lis, S. Upconverting lanthanide fluoride core@shell nanorods for luminescent thermometry in the first and second biological windows: β-$NaYF_4$:Yb^{3+}-Er^{3+}@SiO_2 temperature sensor. *ACS Appl. Mater. Interfaces* **2019**, *11*, 13389−13396.

(42) Zeng, S.; Tsang, M. K.; Chan, C. F.; Wong, K. L.; Hao, J. PEG modified $BaGdF_5$:Yb/Er nanoprobes for multi-modal upconversion fluorescent, *in vivo* X-ray computed tomography and biomagnetic imaging. *Biomaterials* **2012**, *33*, 9232−9238.

(43) Liu, Y.; Ai, K.; Liu, J.; Yuan, Q.; He, Y.; Lu, L. A high-performance ytterbium-based nanoparticulate contrast agent for *in vivo* X-Ray computed tomography imaging. *Angew. Chem., Int. Ed.* **2012**, *51*, 1437−1442.

(44) Yu, S. B.; Watson, A. D. Metal based X-ray contrast media. *Chem. Rev.* **1999**, *99*, 2353−2377.

https://dx.doi.org/10.1021/acs.inorgchem.0c01818
Inorg. Chem. XXXX, XXX, XXX−XXX

(45) Tian, G.; Zheng, X.; Zhang, X.; Yin, W.; Yu, J.; Wang, D.; Zhang, Z.; Yang, X.; Gu, Z.; Zhao, Y. TPGS-stabilized $NaYbF_4$: Er upconversion nanoparticles for dual-modal fluorescent/CT imaging and anticancer drug delivery to overcome multi-drug resistance. *Biomaterials* **2015**, *40*, 107−116.

(46) Shannon, R. D. Revised effective ionic radii and systematic studies of interatomic distances in halides and chalcogenides. *Acta Crystallogr., Sect. A: Cryst. Phys., Diffr., Theor. Gen. Crystallogr.* **1976**, *32*, 751−767.

(47) Zhou, T.; Luo, R.; Li, Y.; Li, T.; Zhao, Y.; Liu, M.; Lai, X.; Bi, J.; Gao, D. Yb^{3+}, Tm^{3+} co-doped β-$NaY_{1-x}Gd_xF_4$ ($0 \leq x \leq 1.00$) microcrystals: Hydrothermal synthesis, evolution of microstructures and upconversion luminescence properties. *J. Lumin.* **2019**, *211*, 363−374.

(48) Yin, W.; Zhao, L.; Zhou, L.; Gu, Z.; Liu, X.; Tian, G.; Jin, S.; Yan, L.; Ren, W.; Xing, G.; Zhao, Y. Enhanced red emission from GdF_3:Yb^{3+}, Er^{3+} upconversion nanocrystals by Li^+ doping and their application for bioimaging. *Chem. - Eur. J.* **2012**, *18*, 9239−9245.

(49) Hu, H.; Xiao, L.; Zhang, X. Synthesis and characterization of Ln,Yb: $BaGdF_5$ (Ln = Er, Ho) nanocrystals by hydrothermal method. Russ. *J. Phys. Chem. A* **2017**, *91*, 2034−2038.

(50) Jiao, Y.; Gao, X.; Lu, J.; Chen, Y.; He, W.; Chen, X.; Li, X.; Li, R. Hydrothermal synthesis of the intense green photoluminescence of hexagonal phase $NaYF_4$:Yb^{3+}/Er^{3+} microcrystals. *J. Alloys Compd.* **2013**, *549*, 245−253.

(51) Pang, X.; Zhang, Y.; Ding, L.; Su, Z.; Zhang, W. F. Upconversion luminescence properties of Er^{3+}-Bi^{3+} codoped $CaSnO_3$ nanocrystals with perovskite structure. *J. Nanosci. Nanotechnol.* **2010**, *10*, 1860−1864.

(52) Park, W. J.; Jung, M. K.; Yoon, D. H. Influence of Eu^{3+}, Bi^{3+} co-doping content on photoluminescence of YVO_4 red phosphors induced by ultraviolet excitation. *Sens. Actuators, B* **2007**, *126*, 324−327.

(53) Hong, F.; Cheng, H.; Liu, G.; Dong, X.; Yu, W.; Wang, J. Controlled morphology, improved photoluminescent properties, and application of an efficient non-rare earth deep red-emitting phosphor. *Inorg. Chem.* **2018**, *57*, 9892−9901.

(54) Zhou, R.; Liu, X.; Wu, Y.; Xiang, H.; Cao, J.; Li, Y.; Yin, W.; Zu, Y.; Li, J.; Liu, R.; Zhao, F.; Liu, Z.; Chen, C.; Gu, Z.; Yan, L.; Zhao, Y. Suppressing the radiation-induced corrosion of bismuth nanoparticles for enhanced synergistic cancer radiophototherapy. *ACS Nano* **2020**, *14*, 13016−13029.

https://dx.doi.org/10.1021/acs.inorgchem.0c01818
Inorg. Chem. XXXX, XXX, XXX−XXX